

PAPER

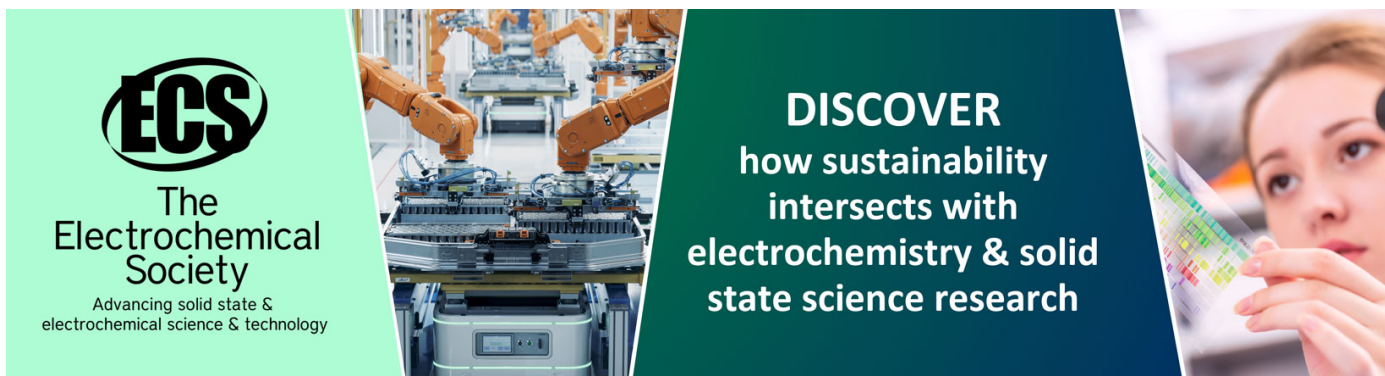
Formation mechanisms of ZnO nanowires on polycrystalline Au seed layers for piezoelectric applications

To cite this article: Clément Lausecker *et al* 2019 *Nanotechnology* **30** 345601

View the [article online](#) for updates and enhancements.

You may also like





- [Shadow mask assisted direct growth of ZnO nanowires as a sensing medium for surface acoustic wave devices using a thermal evaporation method](#)
Ajay Achath Mohanan, R Parthiban and N Ramakrishnan
- [Density-controlled electrochemical synthesis of ZnO nanowire arrays using nanotextured cathode](#)
Hyeonjin Eom, Junyoung Hur, Sang-Keun Sung et al.
- [Diameter-dependent ultra-high thermoelectric performance of ZnO nanowires](#)
Yinan Nie, , Guihua Tang et al.



ECS
The
Electrochemical
Society
Advancing solid state &
electrochemical science & technology

DISCOVER
how sustainability
intersects with
electrochemistry & solid
state science research

Formation mechanisms of ZnO nanowires on polycrystalline Au seed layers for piezoelectric applications

Clément Lausecker^{1,2,3} , Bassem Salem^{2,4} , Xavier Baillin³,
Hervé Roussel¹, Eirini Sarigiannidou¹, Franck Bassani² , Estelle Appert¹,
Sébastien Labau² and Vincent Consonni^{1,4} 

¹ Univ. Grenoble Alpes, CNRS, Grenoble INP, LMGP, F-38000 Grenoble, France

² Univ. Grenoble Alpes, CNRS, LTM, F-38054 Grenoble Cedex, France

³ Univ. Grenoble Alpes, CEA, LETI, F-38000 Grenoble, France

E-mail: bassem.salem@cea.fr and vincent.consonni@grenoble-inp.fr

Received 28 February 2019, revised 24 April 2019

Accepted for publication 29 April 2019

Published 29 May 2019



Abstract

ZnO nanowires are considered as attractive building blocks for piezoelectric devices, including nano-generators and stress/strain sensors. However, their integration requires the use of metallic seed layers, on top of which the formation mechanisms of ZnO nanowires by chemical bath deposition are still largely open. In order to tackle that issue, the nucleation and growth mechanisms of ZnO nanowires on top of Au seed layers with a thickness in the range of 5–100 nm are thoroughly investigated. We show that the ZnO nanowires present two different populations of nano-objects with a given morphology. The majority primary population is made of vertically aligned ZnO nanowires, which are heteroepitaxially formed on top of the Au (111) grains. The resulting epitaxial strain is found to be completely relieved at the Au/ZnO interface. In contrast, the minority secondary population is composed of ZnO nanowires with a significant mean tilt angle around 20° with respect to the normal to the substrate surface, which are presumably formed on the (211) facets of the Au (111) grains. The elongation of ZnO nanowires is further found to be limited by the surface reaction at the *c*-plane top facet in the investigated conditions. By implementing the selective area growth using electron beam lithography, the position of ZnO nanowires is controlled, but the two populations still co-exist in the ensemble. These findings provide an in-depth understanding of the formation mechanisms of ZnO nanowires on metallic seed layers, which should be taken into account for their more efficient integration into piezoelectric devices.

Supplementary material for this article is available [online](#)

Keywords: ZnO nanowires, chemical bath deposition, Au seed layers, heteroepitaxy

(Some figures may appear in colour only in the online journal)

1. Introduction

Piezoelectric devices like piezoelectric nano-generators (PENGs) and sensors including zinc oxide (ZnO) nanostructures have received an increasing interest over the last decade [1–6]. They benefit from the main advantages of ZnO

as an abundant, biocompatible, wide band-gap semiconductor (3.3 eV at room temperature) with relatively high piezoelectric constants ($e_{33} = 1.34 \text{ C/m}^{-2}$ and $e_{31} = -0.57 \text{ C/m}^{-2}$) [7]. By using vertically aligned ZnO nanowire (NW) arrays with high aspect ratios and controlled densities, the piezoelectric effect is further greatly enhanced as compared to the use of bulk ZnO and thin films [8]. Additionally, the use of NWs embedded in a polymer matrix forms a functionally graded

⁴ Authors to whom any correspondence should be addressed.

interface, enhancing both the mechanical properties and electromechanical behavior through the improvement of the strain transfer from one phase to another [9, 10]. The resulting PENGs integrating such morphologically controlled ZnO NW arrays have the potential to autonomously supply low-power miniaturized wearable devices [3]. ZnO NWs can be synthesized by a wide variety of physical and chemical deposition techniques, such as pulsed-laser deposition [11], vapor-phase transport [12], thermal evaporation [13], molecular beam epitaxy [14], standard and metal-organic chemical vapor deposition [15, 16], electrodeposition [17], and chemical bath deposition (CBD) [18]. Increasing attention has been devoted to CBD as a low-temperature and low-cost surface scalable process, which can further be easily implemented on any kind of rigid and flexible substrates [19]. In this technique, the substrate is immersed in a sealed beaker containing the aqueous solution of the appropriate chemical precursors, which is heated at moderate temperature for several hours. A polycrystalline seed layer composed of ZnO nanoparticles (NPs) is usually pre-deposited on the substrate, so that the heterogeneous nucleation of vertically aligned ZnO NWs through its local homoepitaxy is favored over the homogeneous nucleation in aqueous solution [20]. This implies a strong relationship between the structural properties of the ZnO NPs and NWs, which has given rise to many reported investigations to fully elucidate the formation mechanisms of the NWs and to carefully optimize their morphology [20–23].

Nonetheless, metallic seed layers are required for the integration of vertically aligned ZnO NWs into PENGs, where a Schottky like contact with an electrode is needed [24]. ZnO is known to form Schottky contacts with high work function metals, including Pt, Au, Ag, and Pd [25]. Among these metals, Au has shown promising results when used as polycrystalline seed layers for the growth of ZnO NWs by wet chemical methods [26–37], and such NW arrays have successfully been integrated into PENGs [33–35]. However, in the same manner as with polycrystalline ZnO seed layers, a comprehensive and in-depth understanding of the formation of ZnO NWs on polycrystalline Au seed layers is necessary to carefully optimize their morphology (i.e. length, diameter, density, and verticality), as a pre-requisite for enhancing the performances of the related PENGs. The Au seed layers are commonly deposited by vacuum evaporation or sputtering, which typically confer a strongly (111)-oriented polycrystalline structure to the film. The nucleation mechanisms of ZnO NWs on polycrystalline Au seed layers are usually explained by the similar structures of the face-centered-cubic Au (111) and wurtzite ZnO (0001) planes despite a 12.7% lattice mismatch, which could allow for their local heteroepitaxy [26, 28]. Shen *et al* observed a very smooth interfacial region between the Au grains composing the seed layer and the *c*-axis oriented ZnO NWs, suggesting an heteroepitaxial process [38]. However, no advanced characterization could unambiguously show the structural relationship at the interface. A heteroepitaxial process would result in an even stronger influence of the structural properties of the polycrystalline Au seed layers on the morphology of ZnO NWs. Although the effects of the growth conditions (e.g. growth

time and temperature, chemical precursor concentrations) have been reported in the case of the CBD of ZnO NWs on polycrystalline Au seed layers [30, 31, 34], the influence of its structural properties has not been addressed yet. Such investigation has the great potential to provide valuable information on the nucleation and growth mechanisms of ZnO NWs on polycrystalline Au seed layers in order to completely control their morphology and hence to improve the performances of the related PENGs.

Another approach to obtain morphologically controlled ZnO NW arrays is to perform selective area growth (SAG) using advanced lithography techniques. Electron beam lithography (EBL) has already demonstrated the capability to provide well-ordered ZnO NW arrays by CBD on different substrates [39–45]. The nucleation rate needs to be enhanced, when performing the SAG of ZnO NWs on polycrystalline Au seed layers, which is typically achieved by applying an electric field in the chemical bath [46, 47]. However, Zhang *et al* revealed the SAG of ZnO NWs on polycrystalline Au seed layers pre-patterned by EBL without any external electric field by optimizing the growth conditions [48]. These works demonstrate the feasibility to grow ZnO NWs on polycrystalline Au seed layers by SAG, but their resulting morphology is still limited by a lacking in the understanding of their nucleation and growth mechanisms.

In this work, we investigate the influence of the structural properties of the Au seed layers grown by vacuum evaporation on the subsequent nucleation and growth of ZnO NWs by CBD. The structural properties of the polycrystalline Au seed layers are changed by varying its thickness over a broad range of 5–100 nm. The structural relationship with ZnO NWs is investigated by atomic force microscopy (AFM), field-emission scanning electron microscopy (FESEM), x-ray diffraction (XRD), and x-ray pole figure measurements. Additionally, a thorough study of the properties of the Au grain/ZnO NW interfacial region is carried out by transmission electron microscopy (TEM), allowing us to establish a complete nucleation and growth diagram. EBL is eventually used to implement the SAG on top of the pre-patterned polycrystalline Au seed layers as a step forward for their efficient integration into PENGs.

2. Experimental section

2.1. Deposition techniques

In order to remove the native silicon oxide layer, silicon (100) wafers acting as substrates were dipped for 1 min in a buffered hydrofluoric acid solution followed by a deionized water rinsing. Prior to the deposition of the polycrystalline Au seed layers, 10 nm thick Ti layers were deposited to ensure the adhesion of Au on the silicon wafers. Polycrystalline Au seed layers with a thickness of 5, 10, 20, 50, and 100 nm were then deposited by vacuum evaporation at room temperature and at a rate of 0.25 nm s^{-1} by varying the growth time from 20 to 400 s. ZnO NWs were grown by CBD under strictly identical conditions. The samples laid face down in separate sealed beakers containing the aqueous solution of chemical

precursors and were placed for 3 h in an oven kept at 90 °C. The solutions contained 30 mM of zinc nitrate hexahydrate ($\text{Zn}(\text{NO}_3)_2 \cdot 6\text{H}_2\text{O}$, Alfa Aesar) and 30 mM of hexamethylenetetramine (HMTA, $\text{C}_6\text{H}_{12}\text{N}_4$, Sigma Aldrich) dissolved in deionized water. To investigate the nucleation mechanisms, ZnO NWs grown with a shorter growth time of 50 min were formed on 5, 20 and 100 nm thick polycrystalline Au seed layers. Eventually, the SAG of ZnO NWs by CBD using the same conditions, but with a longer growth time of 5 h, was performed on a 5 nm thick polycrystalline Au seed layer pre-patterned by EBL. A 90 nm thick poly(methyl methacrylate) (PMMA) resist was spin-coated on the sample and subsequently patterned by EBL using a JBX-6300FS EBL System. The patterned area presented a $17 \mu\text{m} \times 20 \mu\text{m}$ array of holes with a mean diameter of 60 ± 10 nm and a period of 200 nm.

2.2. Characterization techniques

AFM measurements were performed on the polycrystalline Au seed layers with a Bruker Innova AFM equipment in tapping mode using OTESPA-R3 probe (Bruker) having a tip radius of 7–10 nm. The Au mean grain sizes were extracted using Gwyddion software and deduced from the maximum of the lognormal fit of the size distribution. θ – 2θ XRD measurements with the standard Bragg–Brentano configuration were recorded with a Bruker D8 Advance diffractometer using the Cu $\text{K}\alpha_1$ radiation ($\lambda = 0.15406$ nm). The acquisition range was scanned from 35° to 85° (in 2θ scale) with a step of 0.01° and 3 s by step. From XRD patterns, the mean crystallite size of the polycrystalline Au seed layers was calculated from the Debye–Scherrer equation [49]:

$$\tau = \frac{K\lambda}{\beta \cos \theta},$$

where θ is the experimental Bragg angle of the Au (111) diffraction peak, K is a shape factor equal to 0.9 and β is the full width at half-maximum (FWHM) of the peak corrected by the instrumental broadening. X-ray rocking curves and pole figures were collected with a Siemens D5000 diffractometer using the mean Cu $\text{K}\alpha$ radiation ($\lambda = 0.1544$ nm). The apparatus was equipped with a 4 circle goniometer (i.e. for ω , 2θ , φ and χ), 2.5° Sollers slits, a nickel (Ni) filter and a scintillation detector. The rocking curves were recorded along the Au (111) diffraction peak according to the 00-004-0784 pattern of the International Center of Diffraction Data (ICDD). ω ranged from 5° to 35° with a step of 0.1° and 2.5 s by step. Half of the FWHM was considered as a quantitative measurement of the mosaicity of the Au (111) planes (i.e. its mean tilt angle with respect to the parallel to the surface). The x-ray pole figure patterns were performed along the ZnO (0002) diffraction peak according to the ICDD 00-036-1451 pattern. They were reconstructed from multiple φ -scans (ranging from 0° to 360°) at various χ angles (ranging from 0° to 90°). The mean tilt angle of ZnO NWs was determined by considering half of the FWHM of the main peak. The morphological properties of ZnO NWs were

Table 1. Structural properties of the Au seed layers with a thickness ranging from 5 to 100 nm.

Au thickness (nm)	RMS roughness (nm)	Grain size (nm)	Crystallite size (nm)	Au (111) mosaicity (°)
5	0.15	35.5 ± 1.5	5.5 ± 0.1	6.9 ± 0.2
10	0.19	36.3 ± 1.5	9.6 ± 0.3	3.2 ± 0.1
20	0.26	38.6 ± 1.5	18.5 ± 0.9	2.4 ± 0.1
50	0.60	47.8 ± 1.4	41.5 ± 2.6	2.3 ± 0.1
100	1.27	49.1 ± 1.5	69.0 ± 8.2	1.6 ± 0.1

also investigated with a FEI Quanta 250 FESEM. Top and cross-sectional view of the NWs were recorded to assess their typical dimensions (i.e. length, diameter) and densities. TEM specimens were prepared by focused ion beam (FIB) in a Zeiss NVision40 FIB-SEM microscope. TEM and high-resolution TEM (HRTEM) images were recorded in a JEOL-JEM 2010 microscope operating at 200 kV with a 0.19 nm point-to-point resolution.

3. Results and discussion

3.1. Structural morphology of the Au seed layers

The structural properties of the Au seed layers are presented in table 1 and figures 1–2. The evaporated Au seed layers are deposited on a 10 nm thick Ti adhesion layer that is crystalline and composed of nano-sized grains, as revealed in figure S1 (available online at stacks.iop.org/NANO/30/345601/mmedia). The Au seed layers are polycrystalline and composed of an ensemble of grains that is clearly visible for layers thicker than 20 nm, as shown in figure 1 by AFM images. The root-mean-square (RMS) roughness of the Au seed layers lies in the range of 0.15–1.27 nm and continuously increases as its thickness is increased, indicating a relatively smooth surface. The mean grain size of the Au seed layers follows the same trend and continuously increases from 35.5 ± 1.5 to 49.1 ± 1.5 nm as its thickness is increased. Interestingly, the Au seed layers exhibit a very strong texture along the $\langle 111 \rangle$ direction regardless of its thickness, as revealed in figure 2(a) by the highly pronounced Au (111) and (222) diffraction peaks. No additional diffraction peaks occur in the XRD patterns. This shows that almost all the grains are (111)-oriented from the very first steps of the growth. This strong growth texture is commonly explained as a consequence of the minimization of the free energy of the Au seed layers as the {111} closest-packed planes have the lowest surface energy. In contrast, no contribution from the Ti sublayer to the XRD patterns is revealed. From the FWHM of the Au (111) diffraction peak and Debye–Scherrer equation, the mean crystallite size of the Au seed layers is deduced in the direction perpendicular to the surface and reported in table 1. As expected, it continuously increases from 5.5 ± 0.1 to 69.0 ± 8.2 nm, as the thickness of the Au seed layers is increased. These values typically do not match those extracted from AFM images reporting the mean grain size in the plane of the surface, which is certainly

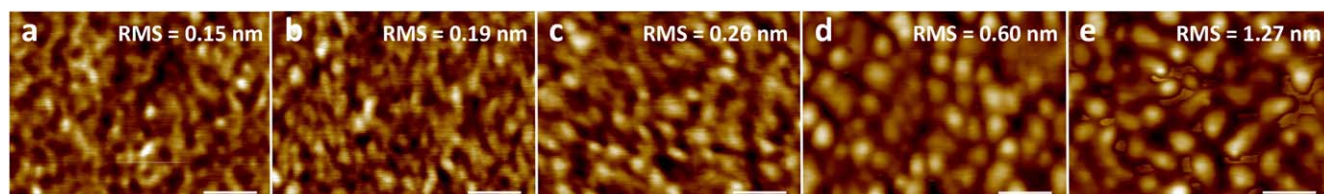


Figure 1. AFM images of the Au seed layers and the corresponding RMS roughness for a thickness of (a) 5 nm, (b) 10 nm, (c) 20 nm, (d) 50 nm, and (e) 100 nm. The scale bar represents 100 nm.

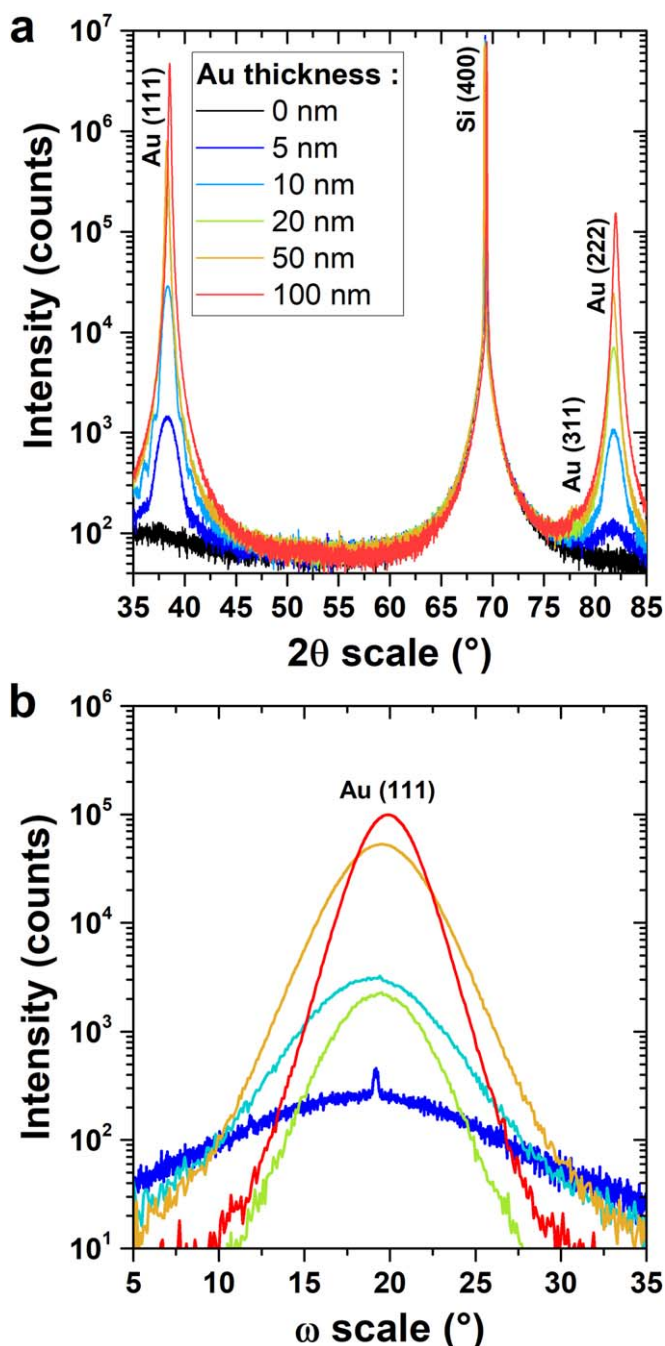


Figure 2. XRD patterns reporting the (a) θ - 2θ scans and (b) rocking curves of the Au seed layers with a thickness ranging from 5 to 100 nm.

related to a tip-surface convolution effect. As the thickness is increased from 5 to 20 nm, the mean crystallite size retains the same values, which indicate that the Au seed layers are composed of one single layer of grains. As the thickness is increased further to 100 nm, the mean crystallite size gets larger than the mean grain size, but much smaller than the thickness of the Au seed layers. This shows that, the grains elongate and follow a columnar shape as the thickness is increased above 50 nm, and that, the Au seed layers are composed of the stacking of several layers of grains. The x-ray rocking curves recorded along the Au (111) diffraction peak are presented in figure 2(b). The mosaicity of the Au (111) planes is deduced from the FWHM of those peaks in table 1. It typically decreases from 6.9 ± 0.2 to $1.6^\circ \pm 0.1^\circ$ as the thickness is increased from 5 to 100 nm. The improved mosaicity indicates that the Au seed layers are progressively self-ordered into better-oriented (111) grains during the growth. One can further notice a narrower satellite Au (111) diffraction peak collected on the 5 nm thick Au seed layer. This may emphasize a greater volume of Au with a lower mosaicity than statistical expectations. Either more grains would have a low mosaicity or the grains with a lower mosaicity would develop at a faster growth rate.

3.2. Effects of the structural morphology of the Au seed layers on the typical dimensions and vertical alignment of ZnO NWs

The structural morphology of ZnO NWs grown by CBD for 3 h on top of the Au seed layers with a thickness ranging from 5 to 100 nm is presented in figure 3 and their typical dimensions are reported in table 2. The mean diameter and length of ZnO NWs were determined from the analysis of cross-sectional view FESEM images while their number density was assessed from the analysis of top-view FESEM images. Overall, ZnO NWs show the typical hexagonal shape, which is related to their wurtzite structure oriented along the polar c -axis. As the thickness of the Au seed layers is increased from 5 to 100 nm, the mean number density of ZnO NWs continuously decreases from 5.7 ± 1.4 to $1.9 \pm 0.9 \mu\text{m}^{-2}$. Correlatively, their mean length increases until saturating from 1.8 ± 0.2 to $2.4 \pm 0.2 \mu\text{m}$. In contrast, the mean diameter of ZnO NWs is much less affected by the variation of the thickness of the Au seed layers and lies in the range of 150 ± 40 to 190 ± 50 nm.

In order to quantitatively assess the vertical alignment of ZnO NWs, x-ray pole figures on the (0002) diffraction peak

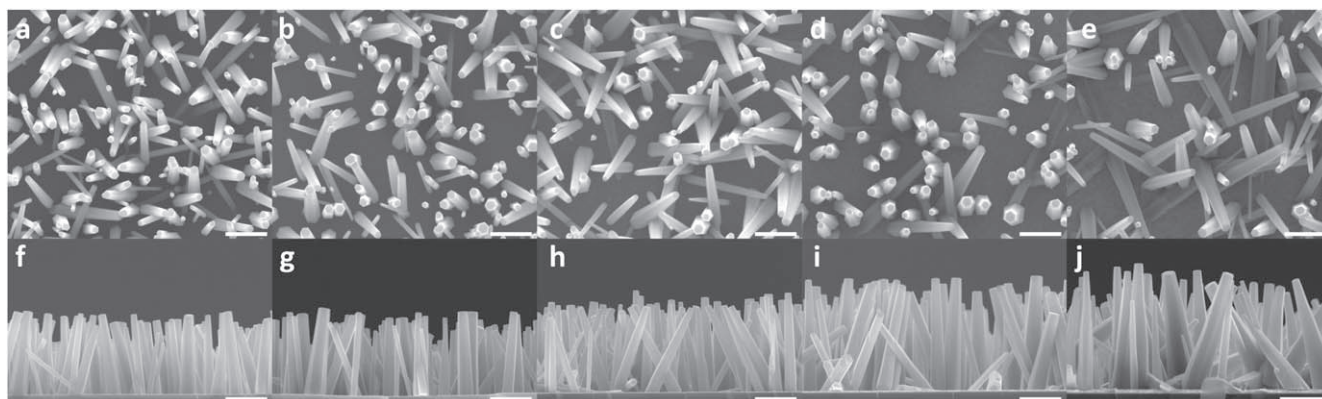


Figure 3. Top-view and cross-sectional view FESEM images of ZnO NWs grown by CBD for 3 h on the (a), (f) 5, (b), (g) 10, (c), (h) 20, (d), (i) 50, and (e), (j) 100 nm thick Au seed layers, respectively. The scale bar represents 1 μm .

Table 2. Structural properties of the ZnO NWs grown by CBD for 3 h on the Au seed layers with a thickness ranging from 5 to 100 nm.

Au thickness (nm)	NW mean diameter (nm)	NW mean length (μm)	NW mean density (μm^{-2})
5	150 ± 40	1.8 ± 0.2	5.7 ± 1.4
10	170 ± 60	1.8 ± 0.2	5.0 ± 0.8
20	150 ± 40	2.1 ± 0.2	3.8 ± 0.8
50	190 ± 50	2.4 ± 0.3	3.6 ± 1.0
100	180 ± 50	2.4 ± 0.2	1.9 ± 0.9

were performed and the related patterns are presented in figures 4(a)–(e). The mean tilt angle of ZnO NWs with respect to the normal to the substrate is deduced from the FWHM of the (0002) diffraction peak and reported in table 3. It is found that the mean tilt angle of ZnO NWs is decreased from $7.01^\circ \pm 0.55^\circ$ to about 3° , as the thickness of the Au seed layers increases from 5 to 100 nm. It is also very close to the corresponding Au (111) mosaicity. These values are further surprisingly low if compared to what is typically obtained following the growth of ZnO NWs by CBD on polycrystalline ZnO seed layers [20]. This indicates that the majority of ZnO NWs gathered in the primary population are very-well aligned vertically with respect to the normal of the substrate. Interestingly, in addition to the primary (0002) diffraction peak centered at $\chi = 0^\circ$, a secondary diffraction peak centered at $\chi \approx 25^\circ$ with an homogeneous intensity along all φ angles is clearly shown in figures 4(a)–(e). The corresponding normalized mean intensity integrated over all φ angles is presented in figure 4(f) and reveals that the secondary diffraction peak occurs regardless of the thickness of the Au seed layers. The positions of the secondary diffraction peaks are listed in table 3. Besides the majority primary population of ZnO NWs that are vertically aligned and whose the verticality is even improved by thickening the Au seed layer, this indicates the existence of a minority secondary population of ZnO NWs with a mean tilt angle in the range of 15.7 ± 0.3 to $26.1^\circ \pm 0.2^\circ$ and with no in-plane orientation, depending on the thickness of the Au seed layers.

3.3. Nucleation and growth mechanisms of ZnO NWs on Au seed layers

3.3.1. Nucleation mechanisms. The majority primary population of ZnO NWs that are vertically oriented has a mean tilt angle very close to the Au (111) mosaicity, suggesting an orientation relationship. A conventional TEM image revealing the stack of the different layers from the silicon wafer to the ZnO NW is shown in figure 5.

The typical interfacial region between a Au (111) grain and a c -axis oriented ZnO NW is presented in figure 6. It is clearly revealed, from the HRTEM image and corresponding Fourier filtering enhancement in figures 6(a) and (b), that the c -axis oriented ZnO NW is heteroepitaxially grown on the Au (111) grain. The Au (111) and ZnO (0002) planes are parallel to each other. A geometrical phase analysis (GPA) was achieved along the $\langle 0002 \rangle$ direction of the ZnO NW [50, 51]. A Gaussian mask with size of 0.5 μm was used to select the frequency g , as illustrated in figure 6(b). The GPA mask was placed on the position of the diffraction spots of the Au (111) and ZnO (0002) planes. The reference region was selected inside the Au seed layer, such that the strain field was set to zero in this area. As a result, the strain field e_{zz} along the c -axis was calculated and reconstructed in the strain map presented in figure 6(c). It is shown that the magnitude of the strain field e_{zz} is about 10% in the ZnO NW with respect to the Au (111) grain. This is very close to the expected lattice mismatch between the bulk Au and the bulk ZnO for this set of selected planes and having the Au seed layer as reference, as $\Delta d = \frac{d_{0002} - d_{111}}{d_{111}} = 10.54\%$ where d_{111} and d_{0002} are the Au (111) and ZnO (0002) interplanar spacings, respectively. The epitaxial strain between the Au (111) grain and c -axis oriented ZnO NW is thus completely relieved, which is presumably achieved elastically through the lateral sidewalls of the ZnO NWs as well as plastically through the formation of extended defects (i.e. dislocations) in that region. The lateral sidewalls are further relatively smooth as emphasized in figure S2 and composed of non-polar m -planes. These results show that the primary population of ZnO NWs is heteroepitaxially formed on top of the Au (111) grains, as

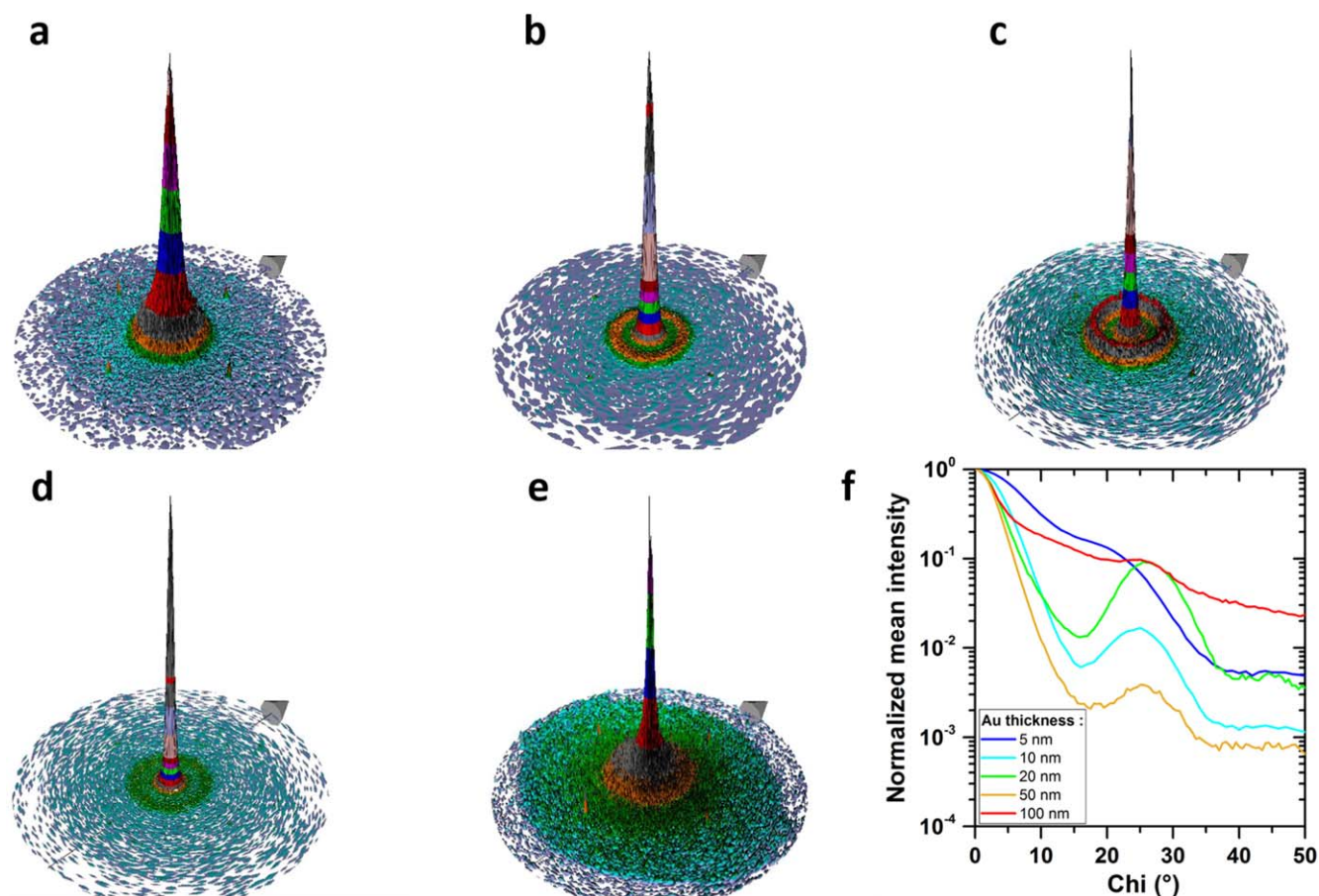


Figure 4. X-ray pole figures recorded on the (0002) diffraction peak of ZnO NWs grown by CBD for 3 h on the (a) 5, (b) 10, (c) 20, (d) 50, and (e) 100 nm thick Au seed layers, respectively. (f) Normalized mean intensity integrated over all φ angles of the corresponding x-ray pole figures.

Table 3. Tilt angles of ZnO NWs grown by CBD for 3 h on the Au seed layers with a thickness ranging from 5 to 100 nm. The tilt angle of the primary population of ZnO NWs corresponds to half of the FWHM of the main (0002) diffraction peak, whereas the tilt angle of the secondary population corresponds to the χ value at which the secondary peak has its maximum intensity.

Au thickness (nm)	Tilt angle of ZnO NWs (°)	
	Primary population	Secondary population
5	7.01 ± 0.55	15.7 ± 0.3
10	4.16 ± 0.38	24.5 ± 0.5
20	3.13 ± 0.61	26.1 ± 0.2
50	2.87 ± 0.19	25.5 ± 0.2
100	3.08 ± 0.60	26.0 ± 0.5

previously suggested in [26, 28]. The heteroepitaxy between ZnO and Au is thus possible, despite the large lattice mismatch involved. Liu *et al* reported for instance the heteroepitaxy of Au NPs on ZnO NW sidewalls and observed an epitaxial relationship between ZnO (1 $\bar{1}$ 01) semi-polar planes and Au (002) planes despite a 17.4% lattice mismatch [52].

The minority secondary population of ZnO NWs with a mean tilt angle lying in the range of 15.7 ± 0.3 to $26.1^\circ \pm 0.2^\circ$ with respect to the normal of the surface,

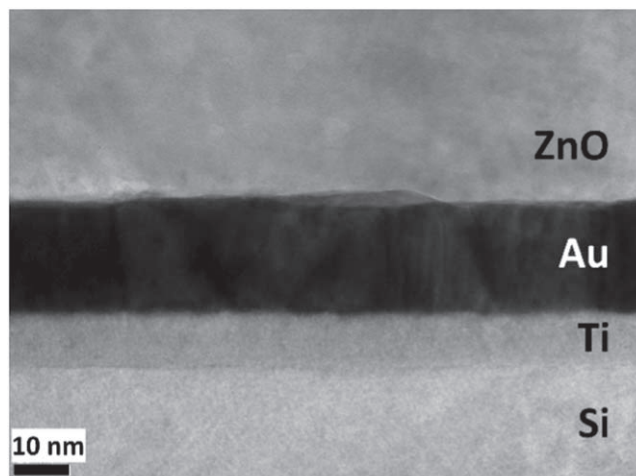


Figure 5. Low magnification TEM image illustrating the stack of the different layers from the silicon wafer to the ZnO NW.

depending on the thickness of the Au seed layers, is expected to follow a distinct nucleation mechanism. This strong misorientation could be induced by the formation of a ZnO NW nucleus on a Au grain exhibiting a facet other than the (111) plane parallel to the surface. In order to minimize surface energy, Au grains typically form grooves at grain

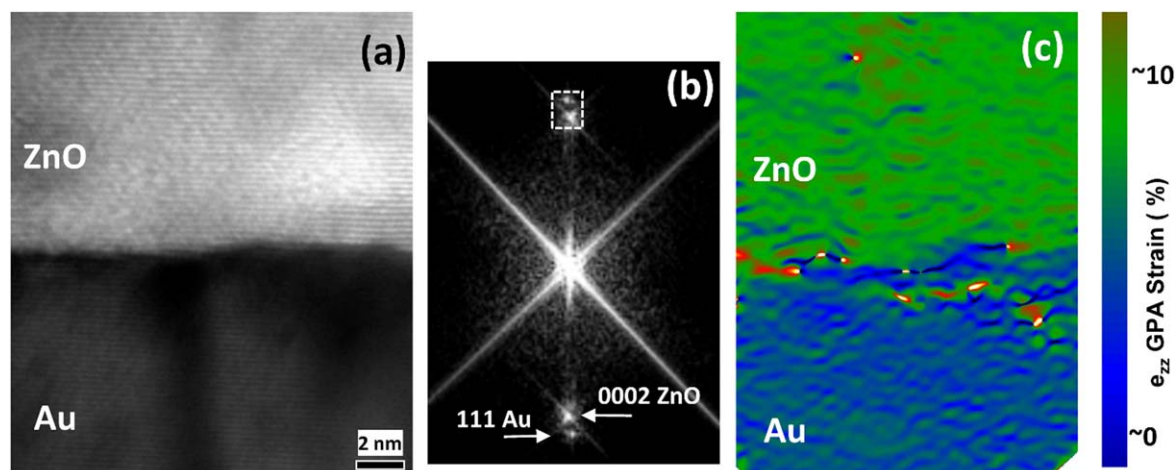


Figure 6. (a) HRTEM image of the interfacial region between a Au (111) grain and a *c*-axis oriented ZnO NW. (b) Corresponding Fourier filtering enhancement. The rectangular area points the position where the GPA mask was placed. (c) Strain map reconstructed from GPA, in which the strain field was set to zero in the Au seed layer.

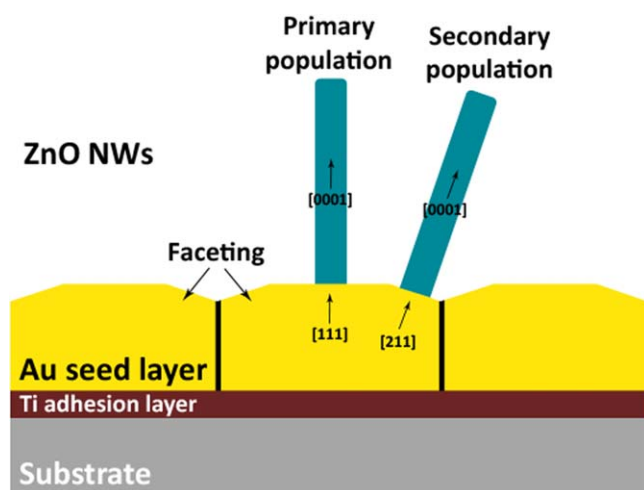


Figure 7. Schematic diagram representing the formation mechanisms of the primary and secondary populations of ZnO NWs. The primary population grows on the (111) facets of the Au (111) grains while the secondary population is expected to grow on the (211) facets of the Au (111) grains.

boundaries, which in turn can lead to the formation of facets on grain edges due to the crystal anisotropy [53]. Such facets can have several possible orientations, mainly depending on the grain size but also on the strain magnitude in the seed layer. One of these possible facets is oriented along the [211] direction [54], which has an inclined angle of 19.5° with respect to the [111] direction. This angle is highly consistent with the mean tilt angle of ZnO NWs in the secondary population, taking into account the mosaicity of the Au grains. This strongly suggests that these ZnO NWs nucleate on the (211) facets of the Au (111) grains, as schematically represented in figure 7. The varying proportion of the primary/secondary populations of ZnO NWs as a function of the thickness of the Au seed layers could arise from the grain size dependent-presence of the (211) facets.

3.3.2. Growth mechanisms. In order to elucidate the growth mechanisms of ZnO NWs on the Au seed layers, the surface reaction-/diffusive transport limited analysis is considered in the following [55]. This analysis states that the *c*-plane growth rate of ZnO NWs is limited either by the surface reaction at the *c*-plane top facet or by the diffusive transport of limited reactants from the bulk solution. The transition between these two growth regimes is mainly dependent upon the *c*-plane top surface area ratio and upon the bulk solution concentration of Zn^{2+} ions [55]. Cossuet *et al* recently determined that for values of *c*-plane top surface area ratios below 0.26 and 0.42 for well-ordered Zn- and O-polar ZnO NWs, respectively, and for the same bulk concentration of Zn^{2+} ions of 30 mM as in the present investigation, the growth of ZnO NWs is limited by the surface reaction [45]. To determine the growth regime at work, ZnO NWs grown by CBD for a reduced duration of 50 min were formed on the 5, 20, and 100 nm thick Au seed layers. The *c*-plane top surface area ratios were carefully measured from top-view FESEM image analysis using the software ImageJ in which a filter was applied to only display the *c*-plane top facets of ZnO NWs. They are found to lie in the range of 0.01–0.03. Such low values suggest that the growth of ZnO NWs on the Au seed layers is limited by the surface reaction at the *c*-plane top facet. The *c*-plane growth rates were calculated by performing the ratio between the mean length of ZnO NWs and their elongation time, which was estimated to be of 10 min as it takes around 40 min to reach the growth temperature of 90°C . The surface reaction-/diffusive transport limited model shows that there exists a linear relationship between the reciprocal *c*-plane growth rate and *c*-plane top surface area ratio, which was experimentally confirmed by Cossuet *et al* in the case of a 30 mM bulk concentration of Zn^{2+} ions [45]. The reciprocal *c*-plane growth rate versus *c*-plane top surface area ratio is plotted in figure 8 and directly compared to the model predictions reported for Zn- and O-polar ZnO NWs grown on pre-patterned Zn- and O-polar ZnO single crystals, respectively.

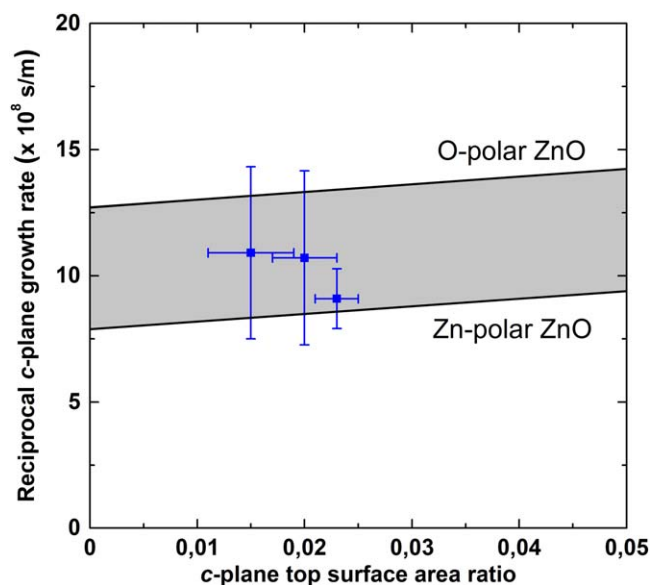


Figure 8. Reciprocal *c*-plane growth rate versus *c*-plane top surface area ratio of ZnO NWs grown by CBD for 50 min on 5, 20, and 100 nm thick Au seed layers. The dark solid lines are the expected fit for Zn and O-polar ZnO NWs, respectively, according to [45]. The bulk solution concentration of Zn^{2+} ions is 30 mM.

Although the polarity of the NWs cannot be deduced in the present case due to the experimental uncertainties, our experimental data are in good agreement with the theoretical model and state that the growth of ZnO NWs is limited by the surface reaction at the *c*-plane top facet. Nonetheless, when considering a longer NW growth time around 3 h, the *c*-plane growth rate gets much lower than the model predictions, the discrepancy being attributed to a very slow nucleation process (leading to a non-constant density over the elongation time) and to dynamical processes in aqueous solution that should be taken into account when the spontaneous growth is employed (in contrast to the SAG in [45]).

3.4. SAG of ZnO NWs on Au seed layers using electron beam lithography

In order to integrate the ZnO NW arrays in PENGs, a precise control over their density and diameter is required to optimize the device performances [8]. The SAG combining EBL and CBD is a potential route to obtain such morphologically controlled ZnO NWs. Prior to the NW SAG, the 5 nm thick Au seed layer was pre-patterned by EBL to form arrays of holes with a desired size and spacing of 60 ± 10 and 200 nm, respectively. The structural morphology of the resulting ZnO NWs grown by CBD for 5 h on this pre-patterned Au seed layer is presented in figure 9(a). One can clearly see that ZnO NWs only form in the $17 \times 20 \mu\text{m}^2$ rectangular area corresponding to the patterned area, which demonstrates the feasibility of the SAG of ZnO NWs on the Au seed layers. The bigger ZnO NWs on the sides of the FESEM image correspond to homogeneously grown ZnO NWs redeposited from the bulk solution. The ZnO NWs present a mean

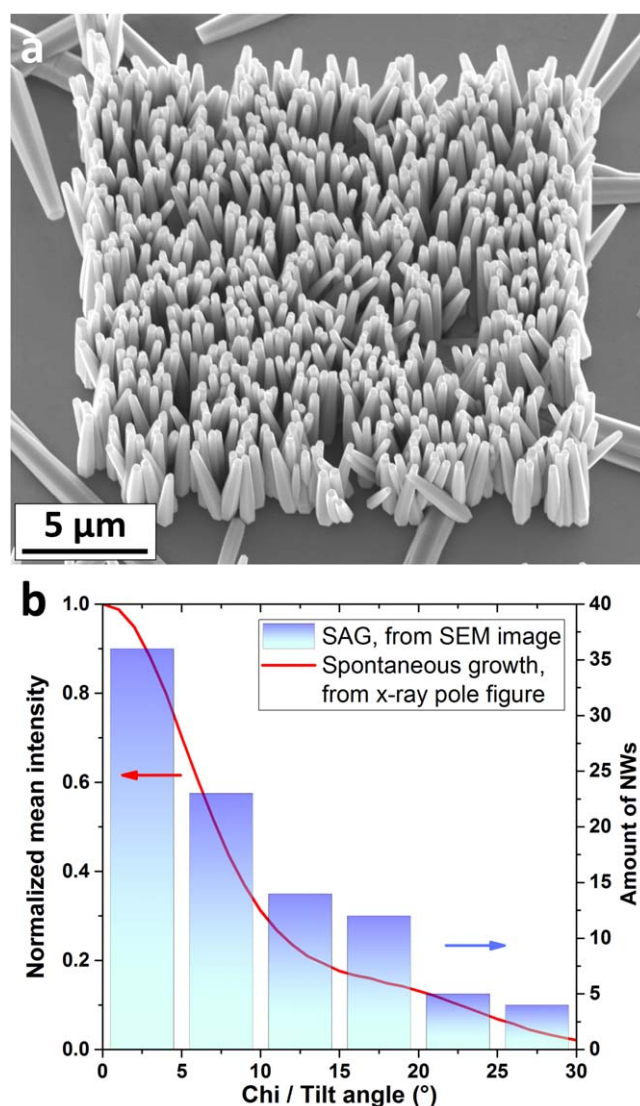


Figure 9. (a) Tilted-view FESEM image of ZnO NWs grown by CBD for 5 h following the SAG on a 5 nm thick Au seed layer pre-patterned by EBL. (b) Normalized mean intensity of the x-ray pole figure on the (0002) diffraction peak recorded on the ZnO NWs grown by CBD following the spontaneous growth on the 5 nm thick Au seed layer in figure 4(f) as a function of the tilt angle (i.e. red solid line). Amount of ZnO NWs grown by CBD following the SAG on a 5 nm thick Au seed layer pre-patterned by EBL as a function of the tilt angle (i.e. blue histogram).

diameter around 280 nm and an apparent number density of $3.8 \mu\text{m}^{-2}$, indicating a good area selectivity but no actual control over their diameter owing to coalescence effects. One can notice that ZnO NWs grown by the SAG are bigger than those grown by the spontaneous growth, which is attributed to a longer growth time. The mean tilt angle of one hundred ZnO NWs was carefully measured from the FESEM image analysis and compared to the x-ray pole figure previously recorded on the pattern-free 5 nm thick Au seed layers, as presented in figure 9(b). Interestingly, the mean tilt angle distributions of the ZnO NWs grown by CBD following both SAG and spontaneous growth show the same trend. This

reveals that the EBL patterning does not affect the nucleation mechanisms of ZnO NWs and hence that both primary and secondary populations are still formed. This result highlights the critical importance of carefully understanding and controlling the nucleation and growth mechanisms of ZnO NWs on Au seed layers, as it can be considered as the most efficient way to thoroughly control their morphology including their diameter and verticality for efficient integration into PENGs. Although the vertical alignment of ZnO NWs is an essential parameter for improving the piezoelectric effect, it should be noted here that the presence of the primary and secondary populations of ZnO NWs with a differential tilt angle in a polymer matrix may all the same be favorable for the mechanical properties and electromechanical behavior [6, 9, 10]. The variation of the thickness of the Au seed layers thus appears as a major parameter to vary the distribution of the primary and secondary populations of ZnO NWs, which could be an efficient tool to tailor the mechanical properties and electromechanical behavior in PENGs.

4. Conclusions

In summary, the formation mechanisms of ZnO NWs grown by CBD on top of polycrystalline Au seed layers grown by vacuum evaporation with a thickness ranging from 5 to 100 nm have thoroughly been investigated. The Au seed layers are basically composed of nano-sized grains strongly oriented along the $\langle 111 \rangle$ direction, as revealed by AFM and XRD measurements. By increasing its thickness from 5 to 100 nm, both the roughness of the Au seed layers and their mean grain size are increased, while the mosaicity of the Au (111) grains is strongly reduced. Correlatively, it has been shown, from FESEM and x-ray pole figure measurements, that the ZnO NW ensemble is composed of two populations of nano-objects with a given morphology. The majority primary population of ZnO NWs is vertically aligned along the c -axis and heteroepitaxially formed on top of the Au (111) grains, as revealed by HRTEM images. The epitaxial strain is completely relieved at the Au/ZnO interface, which is presumably achieved elastically by their smooth lateral sidewalls as well as plastically through the formation of extended defects. In contrast, the minority secondary population of ZnO NWs has a mean tilt angle around 20° with respect to the normal to the substrate surface, which is presumably due to its formation on top of the (211) facets of the Au (111) grains. It has further been revealed that the elongation of ZnO NWs is limited by the surface reaction at the c -plane top facet in the investigated conditions and that its growth rate is overall in agreement with an elongation regime theoretical analysis for the short growth times. The SAG of ZnO NWs using pre-patterned Au seed layers by EBL has eventually been performed, showing the possibility to carefully control their position while forming the two populations of nano-objects. These findings reporting an in-depth understanding of the formation mechanisms of ZnO NWs on Au seed layers reveal the need for optimizing their structural relationship, as an

important step toward their more efficient integration into piezoelectric devices.


Acknowledgments

This work was partially supported by the LabEx Minos under the contract ANR-10-LABX-55-01. C L held a doctoral fellowship from the LabEx Minos. This research has further benefited from some of the characterization equipments of the Grenoble INP—CMTC platform. This work was also partially supported by the French National Research Agency in the framework of the ‘Investissement d’avenir’ program (ANR-15-IDEX-02) through the project CDP NEED and by the French RENATECH network through the CIME-Nanotech and PTA technological platforms in a cleanroom environment. V C also acknowledges the financial support from the French National Research Agency through the project ROLLER (ANR-17-CE09-0033). The authors thank F Robaut from CMTC, Grenoble, France, for the preparation of TEM specimens by FIB.

ORCID iDs

Clément Lausecker  <https://orcid.org/0000-0001-8139-4029>

Bassem Salem  <https://orcid.org/0000-0001-8038-3205>

Franck Bassani  <https://orcid.org/0000-0001-8688-1328>

Vincent Consonni  <https://orcid.org/0000-0003-0171-8746>

References

- [1] Wang Z L and Song J 2006 Piezoelectric nanogenerators based on zinc oxide nanowire arrays *Science* **312** 242–6
- [2] Wang X, Song J, Liu J and Wang Z L 2007 Direct-current nanogenerator driven by ultrasonic waves *Science* **316** 102–5
- [3] Wang Z L 2008 Towards self-powered nanosystems: from nanogenerators to nanopiezotronics *Adv. Funct. Mater.* **18** 3553–67
- [4] Briscoe J and Dunn S 2015 Piezoelectric nanogenerators—a review of nanostructured piezoelectric energy harvesters *Nano Energy* **14** 15–29
- [5] Wang Z, Pan X, He Y, Hu Y, Gu H and Wang Y 2015 Piezoelectric nanowires in energy harvesting applications *Adv. Mater. Sci. Eng.* **2015** 165631
- [6] Malakooti M H, Patterson B A, Hwang H-S and Sodano H A 2016 ZnO nanowire interfaces for high strength multifunctional composites with embedded energy harvesting *Energy Environ. Sci.* **9** 634–43
- [7] Özgür Ü, Alivov Y I, Liu C, Teke A, Reshchikov M A, Doğan S, Avrutin V, Cho S-J and Morkoç H 2005 A comprehensive review of ZnO materials and devices *J. Appl. Phys.* **98** 041301
- [8] Hinchet R, Lee S, Ardila G, Montes L, Mouis M and Wang Z L 2014 Performance optimization of vertical nanowire-based piezoelectric nanogenerators *Adv. Funct. Mater.* **24** 971–7

- [9] Malakooti M H, Zhou Z, Spears J H, Shankwitz T J and Sodano H A 2016 Biomimetic nanostructured interfaces for hierarchical composites *Adv. Mater. Interfaces* **3** 1500404
- [10] Malakooti M H, Zhou Z and Sodano H A 2018 Enhanced energy harvesting through nanowire based functionally graded interfaces *Nano Energy* **52** 171–82
- [11] Sun Y, Fuge G M and Ashfold M N R 2004 Growth of aligned ZnO nanorod arrays by catalyst-free pulsed laser deposition methods *Chem. Phys. Lett.* **396** 21–6
- [12] Huang M H, Wu Y, Feick H, Tran N, Weber E and Yang P 2001 Catalytic growth of zinc oxide nanowires by vapor transport *Adv. Mater.* **13** 113–6
- [13] Pan Z W, Dai Z R and Wang Z L 2001 Nanobelts of semiconducting oxides *Science* **291** 1947–9
- [14] Heo Y W, Varadarajan V, Kaufman M, Kim K, Norton D P, Ren F and Fleming P H 2002 Site-specific growth of ZnO nanorods using catalysis-driven molecular-beam epitaxy *Appl. Phys. Lett.* **81** 3046–8
- [15] Wu J-J and Liu S-C 2002 Low-temperature growth of well-aligned ZnO nanorods by chemical vapor deposition *Adv. Mater.* **14** 215–8
- [16] Park W I, Kim D H, Jung S-W and Yi G-C 2002 Metalorganic vapor-phase epitaxial growth of vertically well-aligned ZnO nanorods *Appl. Phys. Lett.* **80** 4232–4
- [17] Zheng M J, Zhang L D, Li G H and Shen W Z 2002 Fabrication and optical properties of large-scale uniform zinc oxide nanowire arrays by one-step electrochemical deposition technique *Chem. Phys. Lett.* **363** 123–8
- [18] Vayssieres L, Keis K, Lindquist S-E and Hagfeldt A 2001 Purpose-built anisotropic metal oxide material: 3D highly oriented microrod array of ZnO *J. Phys. Chem. B* **105** 3350–2
- [19] Xu S and Wang Z L 2011 One-dimensional ZnO nanostructures: solution growth and functional properties *Nano Res.* **4** 1013–98
- [20] Guillemin S, Consonni V, Appert E, Puyoo E, Rapenne L and Roussel H 2012 Critical nucleation effects on the structural relationship between ZnO seed layer and nanowires *J. Phys. Chem. C* **116** 25106–11
- [21] Guillemin S, Rapenne L, Roussel H, Sarigiannidou E, Brémond G and Consonni V 2013 Formation mechanisms of ZnO nanowires: the crucial role of crystal orientation and polarity *J. Phys. Chem. C* **117** 20738–45
- [22] Guillemin S, Appert E, Roussel H, Doisneau B, Parize R, Boudou T, Brémond G and Consonni V 2015 Controlling the structural properties of single step, dip coated ZnO seed layers for growing perfectly aligned nanowire arrays *J. Phys. Chem. C* **119** 21694–703
- [23] Guillemin S, Parize R, Carabetta J, Cantelli V, Albertini D, Gautier B, Brémond G, Fong D D, Renevier H and Consonni V 2017 Quantitative and simultaneous analysis of the polarity of polycrystalline ZnO seed layers and related nanowires grown by wet chemical deposition *Nanotechnology* **28** 095704
- [24] Liu J, Fei P, Song J, Wang X, Lao C, Tummala R and Wang Z L 2008 Carrier density and Schottky barrier on the performance of DC nanogenerator *Nano Lett.* **8** 328–32
- [25] Allen M W, Alkaisi M M and Durbin S M 2006 Metal Schottky diodes on Zn-polar and O-polar bulk ZnO *Appl. Phys. Lett.* **89** 103520
- [26] Liu R, Vertegel A A, Bohnann E W, Sorenson T A and Switzer J A 2001 Epitaxial electrodeposition of zinc oxide nanopillars on single-crystal gold *Chem. Mater.* **13** 508–12
- [27] Govender K, Boyle D S, O'Brien P, Binks D, West D and Coleman D 2002 Room-temperature lasing observed from ZnO nanocolumns grown by aqueous solution deposition *Adv. Mater.* **14** 1221–4
- [28] Cao B, Cai W, Duan G, Li Y, Zhao Q and Yu D 2005 A template-free electrochemical deposition route to ZnO nanoneedle arrays and their optical and field emission properties *Nanotechnology* **16** 2567–74
- [29] Gao P-X, Lee J L and Wang Z L 2007 Multicolored ZnO nanowire architectures on etched silicon substrates *J. Phys. Chem. C* **111** 13763–9
- [30] Xu S, Lao C, Weintraub B and Wang Z L 2008 Density-controlled growth of aligned ZnO nanowire arrays by seedless chemical approach on smooth surfaces *J. Mater. Res.* **23** 2072–7
- [31] Xu S, Adiga N, Ba S, Dasgupta T, Wu C F J and Wang Z L 2009 Optimizing and improving the growth quality of ZnO nanowire arrays guided by statistical design of experiments *ACS Nano* **3** 1803–12
- [32] Niarchos G, Makarona E and Tsamis C 2010 Growth of ZnO nanorods on patterned templates for efficient, large-area energy scavengers *Microsyst. Technol.* **16** 669–75
- [33] Xu S, Qin Y, Xu C, Wei Y, Yang R and Wang Z L 2010 Self-powered nanowire devices *Nat. Nanotechnol.* **5** 366–73
- [34] Tian J-H, Hu J, Li S-S, Zhang F, Liu J, Shi J, Li X, Tian Z-Q and Chen Y 2011 Improved seedless hydrothermal synthesis of dense and ultralong ZnO nanowires *Nanotechnology* **22** 245601
- [35] Opoku C, Dahiya A S, Oshman C, Cayrel F, Poulin-Vittrant G, Alquier D and Camara N 2015 Fabrication of ZnO nanowire based piezoelectric generators and related structures *Phys. Procedia* **70** 858–62
- [36] Alenezi M R, Henley S J and Silva S R P 2015 On-chip fabrication of high performance nanostructured ZnO UV detectors *Sci. Rep.* **5** 8516
- [37] Boubenia S, Dahiya A S, Poulin-Vittrant G, Morini F, Nadaud K and Alquier D 2017 A facile hydrothermal approach for the density tunable growth of ZnO nanowires and their electrical characterizations *Sci. Rep.* **7** 15187
- [38] Shen L, Bao N, Yanagisawa K, Zheng Y, Domen K, Gupta A and Grimes C A 2007 Direct growth of comet-like superstructures of Au–ZnO submicron rod arrays by solvothermal soft chemistry process *J. Solid State Chem.* **180** 213–20
- [39] Kim Y-J, Lee C-H, Hong Y J, Yi G-C, Kim S S and Cheong H 2006 Controlled selective growth of ZnO nanorod and microrod arrays on Si substrates by a wet chemical method *Appl. Phys. Lett.* **89** 163128
- [40] Xu S, Wei Y, Kirkham M, Liu J, Mai W, Davidovic D, Snyder R L and Wang Z L 2008 Patterned growth of vertically aligned ZnO nanowire arrays on inorganic substrates at low temperature without catalyst *J. Am. Chem. Soc.* **130** 14958–9
- [41] Volk J, Nagata T, Erdélyi R, Bársony I, Tóth A L, Lukács I E, Czigány Z, Tomimoto H, Shingaya Y and Chikyow T 2009 Highly uniform epitaxial ZnO nanorod arrays for nanopiezotronics *Nanoscale Res. Lett.* **4** 699–704
- [42] Erdélyi R, Nagata T, Rogers D J, Teherani F H, Horváth Z E, Lábadí Z, Baji Z, Wakayama Y and Volk J 2011 Investigations into the impact of the template layer on ZnO nanowire arrays made using low temperature wet chemical growth *Cryst. Growth Des.* **11** 2515–9
- [43] Li G P, Jiang L, Wang S J, Sun X W, Chen X and Wu T 2011 Buffer-layer-assisted epitaxial growth of perfectly aligned oxide nanorod arrays in solution *Cryst. Growth Des.* **11** 4885–91
- [44] Consonni V, Sarigiannidou E, Appert E, Bocheux A, Guillemin S, Donatini F, Robin I-C, Kioseoglou J and Robaut F 2014 Selective area growth of well-ordered ZnO nanowire arrays with controllable polarity *ACS Nano* **8** 4761–70
- [45] Cossuet T, Appert E, Thomassin J-L and Consonni V 2017 Polarity-dependent growth rates of selective area grown ZnO nanorods by chemical bath deposition *Langmuir* **33** 6269–79

- [46] Cui J and Gibson U 2007 Low-temperature fabrication of single-crystal ZnO nanopillar photonic bandgap structures *Nanotechnology* **18** 155302
- [47] Weintraub B, Deng Y and Wang Z L 2007 Position-controlled seedless growth of ZnO nanorod arrays on a polymer substrate via wet chemical synthesis *J. Phys. Chem. C* **111** 10162–5
- [48] Zhang S, Shen Y, Fang H, Xu S, Song J and Wang Z L 2010 Growth and replication of ordered ZnO nanowire arrays on general flexible substrates *J. Mater. Chem.* **20** 10606
- [49] Scherrer P 1918 Bestimmung der Grösse und der inneren Struktur von Kolloidteilchen mittels Röntgenstrahlen *Nachrichten Von Ges. Wiss. Zu Gött.—Math.-Phys. Kl* 98–100
- [50] Rouvière J L and Sarigiannidou E 2005 Theoretical discussions on the geometrical phase analysis *Ultramicroscopy* **106** 1–17
- [51] Hýtch M J, Snoeck E and Kilaas R 1998 Quantitative measurement of displacement and strain fields from HREM micrographs *Ultramicroscopy* **74** 131–46
- [52] Liu J, Qiao B, Song Y, Huang Y and Liu J (J) 2015 Hetero-epitaxially anchoring Au nanoparticles onto ZnO nanowires for CO oxidation *Chem. Commun.* **51** 15332–5
- [53] Thompson C V 2012 Solid-state dewetting of thin films *Annu. Rev. Mater. Res.* **42** 399–434
- [54] Barmparis G D and Remediakis I N 2012 Dependence on CO adsorption of the shapes of multifaceted gold nanoparticles: a density functional theory *Phys. Rev. B* **86** 085457
- [55] Cheng J J, Nicaise S M, Berggren K K and Gradečak S 2016 Dimensional tailoring of hydrothermally grown zinc oxide nanowire arrays *Nano Lett.* **16** 753–9